JOURNAL OF GEOPHYSICAL RESEARCH, VOL. 117, E02005, doi:10.1029/2011JE003831, 2012

Local lunar gravity field analysis over the South Pole-Aitken basin from SELENE farside tracking data

Sander Goossens,[1,2,3] Yoshiaki Ishihara,[1] Koji Matsumoto,[1] and Sho Sasaki[1]

Received 16 March 2011; revised 22 November 2011; accepted 13 December 2011; published 14 February 2012.

[1] We present a method with which we determined the local lunar gravity field model over the South Pole-Aitken (SPA) basin on the farside of the Moon by estimating adjustments to a global lunar gravity field model using SELENE tracking data. Our adjustments are expressed in localized functions concentrated over the SPA region in a spherical cap with a radius of 45° centered at (191.1°E, 53.2°S), and the resolution is equivalent to a 150th degree and order spherical harmonics expansion. The new solution over SPA was used in several applications of geophysical analysis. It shows an increased correlation with high-resolution lunar topography in the frequency band l = 40–70, and admittance values are slightly different and more leveled when compared to other, global gravity field models using the same data. The adjustments expressed in free-air anomalies and differences in Bouguer anomalies between the local solution and the a priori global solution correlate with topographic surface features. The Moho structure beneath the SPA basin is slightly modified in our solution, most notably at the southern rim of the Apollo basin and around the Zeeman crater.

Citation: Goossens, S., Y. Ishihara, K. Matsumoto, and S. Sasaki (2012), Local lunar gravity field analysis over the South Pole-Aitken basin from SELENE farside tracking data, *J. Geophys. Res.*, *117*, E02005, doi:10.1029/2011JE003831.

1. Introduction

[2] The gravity field of a planetary body is often expressed in globally supported spherical harmonics, since these functions arise naturally from Laplace's equation expressed in spherical coordinates. Their global support however means that a large expansion in spherical harmonics is needed to describe small-scale structures, which results in the need to estimate a large amount of coefficients from data. Depending on the data density which may vary geographically, this is not always possible or stable. In those cases, either smoothed global solutions are obtained by applying regularization of the ill-posed inverse problem in the form of a Kaula rule [*Kaula*, 1966] (which constrains each coefficient to zero with a given uncertainty, thus suppressing spurious power in especially the higher degrees), or, alternatively, different representations that describe the gravity signal locally, at smaller scales, can be used. A variety of representations exist and they have been applied successfully to data from satellites orbiting many different planetary bodies. To list but a few examples: the use of mass concentrations (mascons) to describe gravity on the Moon [*Muller and Sjogren*, 1968], or on Earth using recent GRACE data [*Rowlands et al.*, 2010], analysis of line-of-sight accelerations or Doppler residuals for Venus using gravity disturbances [e.g., *Barriot and Balmino*, 1992], and estimating mass anomalies on Jupiter's moon Ganymede [*Anderson et al.*, 2004; *Palguta et al.*, 2006]. Furthermore, *McKenzie and Nimmo* [1997] introduced a method to use line-of-sight accelerations to directly estimate the admittance between gravity and topography locally, from which elastic thickness estimates can be derived. This method was applied to lunar data by *Crosby and McKenzie* [2005].

[3] The lunar gravity field seems especially suitable for using local methods, because the density of available tracking data has been extremely asymmetrical: standard 2-way and 3-way tracking from Earth stations (where the uplink and downlink stations are either the same or different, respectively) leaves a gap in tracking over the farside of the Moon due to the 1:1 spin-orbit resonance of the Earth-Moon system. The Lunar Prospector (LP) mission (1998–1999 [*Binder*, 1998]) flew at altitudes as low as 15 km in its extended mission, resulting in an excellent coverage of the nearside with high-quality tracking data. Despite the farside gap, high resolution models with a spherical harmonics expansion up to a maximum degree of 165 were determined from the tracking data by making use of the aforementioned Kaula rule [*Konopliv et al.*, 2001]. However, it was also realized that the full signal in the tracking data could not be accounted for even with these large expansions, as significant signatures were reported to be seen in the data residuals [*Konopliv et al.*, 2001]. This has lead to several recent analyses using local representations of the gravity field over

[1]RISE Project, National Astronomical Observatory of Japan, Oshu, Japan.
[2]CRESST/Planetary Geodynamics Laboratory, NASA Goddard Space Flight Center, Greenbelt, Maryland, USA.
[3]Department of Physics, University of Maryland, Baltimore County, Baltimore, Maryland, USA.

0148-0227/12/2011JE003831

the nearside of the Moon: *Sugano and Heki* [2004a, 2004b] used line-of-sight accelerations to estimate mass anomalies on the nearside of the Moon, while *Goossens et al.* [2005a, 2005b] used Doppler data residuals directly to estimate gravity anomalies on the lunar surface. Again using line-of-sight accelerations, *Han* [2008] employed localized basis functions to estimate regional gravity fields on the nearside of the Moon for four locations, up to a resolution in spherical harmonics comparable to degree and order 200, and recently *Han et al.* [2011] updated this analysis to include the whole of the nearside at the same resolution.

[4] The farside gap in tracking data was only recently largely filled by the Japanese SELENE mission [*Kato et al.*, 2010], which employed 4-way Doppler data [*Namiki et al.*, 1999] between a relay satellite in a highly elliptical (polar) orbit and a main orbiter in a circular (also polar) orbit at an average altitude of 100 km above lunar surface while the latter was over the farside. This has resulted in lunar gravity field models expressed in spherical harmonics up to a maximum degree and order of 100 [*Namiki et al.*, 2009; *Matsumoto et al.*, 2010]. These models improved the view of farside gravity dramatically, revealing farside free-air gravity anomalies of large impact basins as negative rings with central highs, unlike their counterparts on the nearside of the Moon.

[5] In this paper, we have used the farside Doppler data from SELENE to investigate whether we can extract more information from them than can be modeled with global spherical harmonics. The apolune of Rstar, the relay satellite involved in the 4-way tracking, was located over the southern hemisphere of the farside, resulting in a denser data coverage there [*Matsumoto et al.*, 2010]. Figure 1 shows the 4-way residuals with respect to the SELENE lunar gravity field model SGM100h [*Matsumoto et al.*, 2010], together with the topography as measured with the laser altimeter (LALT) on-board SELENE [*Araki et al.*, 2009]. A model of degree and order 100 in spherical harmonics already pushes the limits of what can be resolved from an altitude of 100 km above lunar surface, but the data coverage and remaining residuals as shown in Figure 1 indicate that there is still something to be gained from a localized analysis, either in terms of obtaining an adjustment with higher resolution, or in terms of redistributing the information in the spectral domain. In addition, the southern hemisphere of the Moon is dominated by the South Pole-Aitken (SPA) basin, the largest impact basin in the solar system (or second largest if the northern lowlands of Mars are counted as an impact basin). A localized analysis of this area might provide information for studying the structure of large impact basins, especially at smaller scales inside the basin.

[6] For our analysis, we express the gravitational potential with localized spherical harmonic functions as described by *Han* [2008], which in turn was based on localized analysis on the sphere as given by *Wieczorek and Simons* [2005], *Simons et al.* [2006], and *Simons and Dahlen* [2006]. Using SELENE tracking data over only the area of interest, we estimate adjustments to the coefficients of these localized functions, rather than estimating adjustments to the coefficients of a spherical harmonic expansion directly. We compare our localized solution to solutions obtained from common global spherical harmonics, and we evaluate the performance of our solution in geophysical analysis using high resolution topography of the Moon.

[7] This paper is structured as follows. We first introduce the data and methods in section 2, and in section 3 we include a benchmark test with LP extended mission data to establish the validity of the method and its implementation. In section 4 we show the results we obtained for the SPA area. The performance of the method is discussed in section 5, followed by the conclusions in section 6.

2. Data and Methods

[8] The tracking data we use will be the data from SELENE (apart from our benchmark test case using LP data as described in section 3). The main interest is in the SPA area, which means that the focus will be on using SELENE 4-way data. However, 2-way data are also available, because a satellite can still be tracked from Earth beyond the limbs and poles of the Moon because of lunar librations. For instance, Figure 1 showed 4-way residuals with several gaps close to the south pole, which will be filled with 2-way data. This also means that there is a lot of LP data over the south pole, but for reasons explained in section 5 we did not include them in our local analysis.

[9] The SELENE Doppler tracking data have a count interval of 10 s. In order to try and obtain more high-resolution information from them, it is possible to use shorter count intervals, but since that will also increase the noise level on the data, we did not pursue this here. Tracking data are processed with the GEODYN II software [*Pavlis et al.*, 2006]. While acceleration data as derived from Doppler residuals have proven to be a very powerful data type for local analysis, we chose for an integrated approach, where the local adjustments are estimated from the tracking data residuals directly. This choice was driven by the fact that the SELENE 4-way data are integrated data, i.e., they consist of the accumulated Doppler shift between the various links. There was no time-tagging for the separate links from which one could isolate only the Doppler shift between relay and main satellite. Our processing of the tracking data, in terms of precision force and measurement modeling, as well as that in terms of which parameters are estimated, is exactly the same as that described by *Matsumoto et al.* [2010]. The difference between the approach described there and the one adopted in this work lies in the way that the gravity parameters are estimated.

[10] Our localized representation of the gravity potential is based on the work of *Han* [2008] (and references therein), where Slepian functions were used to estimate the gravity field over certain areas on the nearside of the Moon from LP line-of-sight accelerations. The Slepian functions are formed from linear combinations of spherical harmonics. For clarity, we repeat the basic transformations between the two sets here, and refer to the aforementioned literature for the details.

[11] A function $f(\theta, \lambda)$ on the sphere is expressed in spherical harmonics as

$$f(\theta,\lambda) = \sum_{l=0}^{L} \sum_{m=-l}^{l} u_{lm} \bar{Y}_{lm} \tag{1}$$

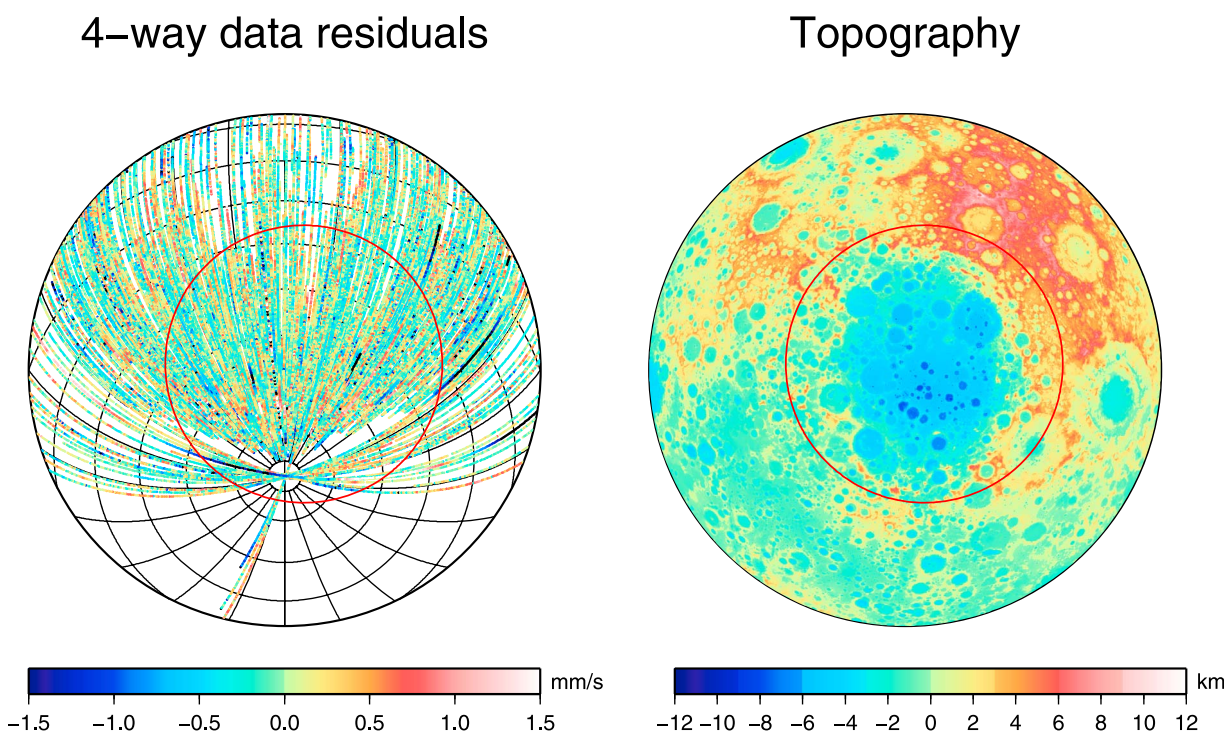

Figure 1. Residuals of 4-way tracking data with respect to the SGM100h model, with the focus on the SPA region (indicated by a red circle with a spherical radius of 45° centered at 191.1°E, 53.2°S). Topography from SELENE altimetry is also shown.

where θ is the co-latitude, λ the longitude, l and m are the degree and order, respectively, L is the maximum degree of the expansion, u_{lm} are the coefficients, and $\bar{Y}_{lm}(\theta, \lambda)$ are the normalized spherical harmonics functions. This same function $f(\theta, \lambda)$ can be expressed in the alternative basis of Slepian functions as

$$f(\theta, \lambda) = \sum_{n=1}^{(L+1)^2} v_n g_n(\theta, \lambda) \tag{2}$$

with different coefficients v_n and Slepian basis functions $g_n(\theta, \lambda)$ [e.g., *Simons and Dahlen*, 2006; *Han*, 2008]. These new basis functions $g_n(\theta, \lambda)$ can also be expressed in a spherical harmonics expansion

$$g_n(\theta, \lambda) = \sum_{l=0}^{L} \sum_{m=-l}^{l} g_{n,lm} \bar{Y}_{lm}(\theta, \lambda). \tag{3}$$

[12] Equation (3) shows the transformation between the bases of spherical harmonics and Slepian functions. To achieve the desired localization of the Slepian functions, the coefficients $g_{n,\,lm}$ are determined from maximizing the ratio between the energy within the desired area, and the energy over the entire sphere (this ratio is also denoted as concentration factor). As discussed by *Wieczorek and Simons* [2005], this can be posed as an eigenvalue problem, where the concentration factors are obtained from the resulting eigenvalues, and the Slepian coefficients $g_{n,\,lm}$ are given by the accompanying eigenvectors. Finally, in the case of the function $f(\theta, \lambda)$ of equation (2), the coefficients v_n for this expansion can then be found from the Slepian coefficients $g_{n,\,lm}$ and the spherical harmonics coefficients u_{lm} following [*Han*, 2008]

$$v_n = \sum_{l=0}^{L} \sum_{m=-l}^{l} u_{lm} g_{n,lm} \tag{4}$$

This results in two equivalent expressions in different basis functions.

[13] *Han* [2008] then separates the spherical harmonic functions into two parts u_{lm}° and $u_{lm}^{\perp}$ (or, equivalently, u_1 and u_2, as we will call them later), with the former consisting of those spherical harmonics concentrated in the desired area up to a chosen concentration factor γ_0 (i.e., the concentration factor for the nth Slepian function satisfies $\gamma_n \geq \gamma_0$), and the latter consisting of the remaining functions outside the chosen area. The full gravitational potential u_{lm} satisfies $u_{lm} = u_{lm}^{\circ} + u_{lm}^{\perp}$. Following equation (4), the spherical harmonics expansion can thus be transformed into Slepian functions using a linear transformation $\mathbf{u} = \mathbf{G}\mathbf{v}$, with $\mathbf{u}$ consisting of the vector of spherical harmonic coefficients u_{lm}, $\mathbf{v}$ consisting of the vector of Slepian coefficients v_n, and $\mathbf{G}$ the transformation matrix between them. By splitting this into the two areas according to:

$$\mathbf{u} = \mathbf{u}_1 + \mathbf{u}_2 = [\mathbf{G}_1\, \mathbf{G}_2] \begin{bmatrix} \mathbf{v}_1 \\ \mathbf{v}_2 \end{bmatrix} \tag{5}$$

Han [2008] then estimated only the Slepian coefficients $\mathbf{v}_1$, i.e., only those that have their concentration in the desired area, using line-of-sight accelerations as the data type. This work was further expanded to global lunar gravity

field modeling from dynamically created normal equations (see below) by applying localized constraints based on this principle by *Han et al.* [2009], and these localized constraints were applied to the full set of NASA Moon orbiter tracking data by *Mazarico et al.* [2010]. In addition, *Han et al.* [2011] recently used the method of *Han* [2008] to estimate the gravity field for the whole nearside of the Moon, again from line-of-sight accelerations. In our analysis, we follow the same principle of dividing the spherical harmonics coefficients into two parts: the main part that we are interested in is concentrated over the SPA area, and the remaining coefficients describe the potential outside of this area.

[14] Because the focus is on a relatively small area on the Moon, long-wavelength signals might not be recovered or represented well in this method. This was noted by *Han* [2008], where it was shown that including the lower spherical harmonics degrees into the localized representation introduced an error of several tens of mGal (1 mGal = 10^{-5}m/s^2), whereas this error was much smaller when components with degrees higher than 30 were used, in the case of a spherical cap with a radius of 20°. This is thus an error of the representation form. We found similar issues in our local solutions, which are created from the localized a priori model plus the estimated adjustments. If the lower degrees of the a priori model were included in the localized a priori part of the constructed solution, we found a strong north-south component in the recovered anomalies that disappeared when the lower degrees were not included. We thus do not include the lower degrees of the a priori model in the localization. Instead, when we reconstruct the full gravity signal in standard spherical harmonics, we add the (global) a priori model up to $l = 30$ after the estimation. There is however one caveat when applying this remove-restore technique: the local basis functions have power over all the degrees, so the adjustment, when transformed back to standard spherical harmonics, will show non-zero signal for $l < 30$. We found however that the amplitude of the adjustments below $l = 30$ is small, at an RMS (root-mean square) of around 2 mGal, and the performance of the model as discussed later in sections 4.3 and 4.4 was unaffected. We also tried to mitigate the effect on the lower degrees in other ways, by generating the design matrix $\mathbf{A}$ with only entries for coefficients with $l \geq 30$, or by band-limiting the transformation matrix $\mathbf{G}$, to span only the range $30 \leq l \leq L$, which makes sure that coefficients with $l < 30$ do not get adjusted. The latter requires special attention: as pointed out by *Wieczorek and Simons* [2005] and *Simons et al.* [2006], the eigenvectors needed to create the localized basis functions are most easily found from a tridiagonal matrix that commutes with the localization matrix, following results by *Grünbaum et al.* [1982]. This works for the full spherical harmonics range, but for the limited range $30 \leq l \leq L$, one has to resort to a direct computation of the localization matrix, and determine the eigenvectors from this matrix rather than from the tridiagonal one. *Wieczorek and Simons* [2005] point out that this might be less stable, but we encountered no discernible differences. Both methods however (limiting the range of the partials, or that of the transformation matrix) did not lead to large differences between solutions. They were again at an RMS of a few mGal, and this shows that the residuals themselves as used in the adjustment already mostly have their signal confined to the high-frequency part of the gravity spectrum. We thus assume that the lower degrees of the gravity field model are already determined from a global rather than a local analysis.

[15] We use a dynamical approach to process the tracking data. The data are divided into continuous time spans called arcs, during which the orbit is integrated using precision force modeling, and parameters valid for that arc only (such as initial state vector adjustments, measurement biases, nonconservative force model coefficients) are adjusted. Once these are converged (typically when the change in the weighted root-mean square of data residuals, consisting of the difference between the observations and those computed from precision modeling, is less than 2% between iterations), we generate the design matrix for the data used in the arc. The design matrix describes how the data depend on the model coefficients, and in standard linear form this is written as $\mathbf{y} = \mathbf{A}\,\mathbf{u} + \mathbf{e}$. Here, the vector $\mathbf{y}$ contains the data residuals, $\mathbf{u}$ is the vector of adjustments to the aforementioned spherical harmonics coefficients that are to be estimated, $\mathbf{e}$ are the data errors, and $\mathbf{A}$ is the design matrix that contains the partials of the observations with respect to the estimation parameters. This estimation problem is often solved using least-squares, which results in the need to form normal matrices, which are given as $\mathbf{A}^T\mathbf{C}_d^{-1}\mathbf{A}$, where ^{T} denotes the transposed of a matrix, $^{-1}$ the inverse, and $\mathbf{C}_d$ is an a priori covariance matrix for the data.

[16] For standard global gravity field determination, this normal matrix is formed from the complete design matrix $\mathbf{A}$ containing all the data included in the arc. In our localized approach however, we use all the data to converge the arcs, and then we select only the data over the area of interest for the formation of a reduced design matrix $\mathbf{A}_{\mathrm{red}}$. We use only the data over the area of interest because in general those residuals are mostly affected by the gravity of features directly beneath them (depending on the data type used). This does mean that at the boundary the solution will be affected by features just outside of the area of interest. We discuss this in sections 3 and 4.3. We then use this reduced design matrix to form a normal matrix, and then proceed as usual by aggregating the normal matrices of all arcs involved, using the SOLVE software [*Ullman*, 2002]. In the case that there are both arc and common parameters (those valid and constant throughout all arcs, such as the gravity field coefficients) present, the arc parameters can be eliminated through partitioning [e.g., *Kaula*, 1966]. We then transform the combined normal matrix following equation (5), and estimate only the coefficients of $\mathbf{v}_1$ which are concentrated over the same area as where we collected the data. This is akin to a truncated singular value decomposition approach [e.g., *Menke*, 1989], where only those coefficients that are observable from the data (i.e., having non-zero singular values) are estimated.

[17] As pointed out by *Simons et al.* [2006], and stressed also by *Han* [2008], the use of Slepian functions that are concentrated over a certain area requires far less coefficients than when a full spherical harmonics expansion is used to obtain the same resolution. This also means that less coefficients need to be adjusted from the data, which in general makes the inverse problem more stable, provided of course that the data actually have the information that is to be extracted. By choosing only data over the area, we also

reduce the number of computations that are needed to form the normal matrices per arc. In this way one is able to compute local solutions with high resolution much faster than global solutions with a similar resolution. Another advantage of the Slepian functions is that they can be transformed back and forth between spherical harmonics, which makes them easy to use with existing tracking data processing tools that are based on a spherical harmonics expansion of the gravity field.

3. Benchmark Test With LP Data Over Mare Serenitatis

[18] In order to test the suggested method and its implementation, we created a benchmark test for a case where the gravity field of the Moon is well-known: over the nearside of the Moon. We chose to test the method over the Mare Serenitatis area, using the same approach as was done by *Goossens et al.* [2005b], where the Lunar Prospector extended mission data over this area were used for local gravity adjustments. LP extended mission data were collected from January until July 1999, at an average spacecraft altitude of 30 km [*Konopliv et al.*, 2001]. These data thus contain a lot of gravity field information at the short wavelengths. By using a pre-LP gravity field model in the processing, we can compare our local solution with known high-resolution global LP models, and thus we can infer whether or not the suggested method can extract the information that is in the tracking data. Because we use real data directly rather than conducting simulations, we can not quantify the recovery error, but this does give us the advantage of directly knowing how the method performs in a real-data environment, while the use of the older gravity field model ensures that we can also test whether the gravity field can be recovered at high resolution. We also do a similar test for our area of interest with the SELENE data, described in section 5.2, although that test is more meant to probe the influence of the a priori model used, rather than to serve as a benchmark test.

[19] We used the same short-arc approach as used by *Goossens et al.* [2005b], where LP extended mission tracking data were processed in short batches, when the satellite was over the Serenitatis area. This leads to arcs of typically ten minutes. We start with an estimate of the initial state that has been determined from longer arcs, using a high-resolution LP gravity model (LP150Q, a follow-up to the 165th degree and order model called LP165P described by *Konopliv et al.* [2001]; the LP150Q model can be found through http://pds-geosciences.wustl.edu/missions/lunarp/shadr.html). Starting from this estimate minimizes initial orbit errors. We then process the short-arcs with the pre-LP GLGM-2 lunar gravity field model [*Lemoine et al.*, 1997] as a priori model. This model shows a much smoother signal for Mare Serenitatis than the LP models. While processing the tracking data with GLGM-2, we fixed some of the Keplerian orbit elements in order to ensure convergence of the short-arc orbit determination problem. Fixed parameters were the same as those of *Goossens et al.* [2005b]: the eccentricity, ascending node, and argument of pericenter. We also noted that the range data are not as sensitive to local gravity variations as the Doppler data, since including the range data distorted the solutions. Doppler data have a better sensitivity, while derived (line-of-sight) accelerations as applied in many examples (mentioned in the introduction) are likely to be more superior, as is especially shown in the recent results of *Han et al.* [2011], where high correlations between gravity and topography are achieved from line-of-sight acceleration data.

[20] We estimate gravity field coefficients equivalent to a spherical harmonics resolution of degree and order 100, using Slepian functions concentrated in a spherical cap of 20° radius, centered around (18°E, 25°N). As described above in section 2, we do not adjust coefficients up to degree $l = 30$. The used concentration factor was 0.0001, and this leads to having to estimate 477 Slepian coefficients. For comparison, a global spherical harmonics model up to degree and order 100 contains 10,197 coefficients. The gravity anomaly solution of *Goossens et al.* [2005b] contained 806 discrete anomalies in 1° × 1° blocks, over a square area (ranging from 5°–30° in longitude, and from 10°–40° in latitude). Tracking data residuals inside this area were used in the estimation process. Because the LP extended mission data were collected at a low altitude, downward continuation has only a small effect on the errors in the solution, and the local solutions can be obtained without any kind of regularization to stabilize the inverse problem [*Sugano and Heki*, 2004a; *Goossens et al.*, 2005a, 2005b; *Han*, 2008].

[21] Figure 2 shows gravity anomalies over the Serenitatis area, computed from either GLGM-2, LP150Q, or from the newly estimated model, with all expansions evaluated up to their respective maximum degree and order. It is immediately clear that the local solution resembles that of LP150Q much more than it resembles the smooth GLGM-2 solution, as the increase in resolution inside the Serenitatis mascon is readily confirmed. The local solution also resolves the area around the mascon better than GLGM-2 does, when compared with LP150Q: the negative anomalies surrounding the mascon come out clearer, and they correlate well with the signal as seen in the anomalies from LP150Q.

[22] Figure 3 shows the anomaly differences between the local solution and anomalies from either GLGM-2 or LP150Q. In addition, to assess boundary effects it also shows the difference between two local solutions with the functions concentrated in a spherical cap of either 20° or 10°. The differences with anomalies from GLGM-2 (which are in fact the adjustments estimated from the data) especially indicate that the extra signal from the data was extracted as there is clear structure visible in the differences. Differences with LP150Q show remaining signal as well, extending into the mascon itself, although most differences are concentrated at the boundaries. This is mostly due to boundary effects that are often present in local solutions, and which arise because although data are mostly affected by the gravity of features directly beneath them (as stated earlier), they also carry information from the surrounding area. Because we used the same processing (including the same way to generate the tracking data residuals) as *Goossens et al.* [2005b], which used spacecraft tracks covering the square area listed above, the data do not fully cover the chosen spherical cap area and this exacerbates the boundary effects. In order to assess the influence of data coverage, we also created a solution that estimated only coefficients in a spherical cap of 10°. This solution is still sensitive to boundary effects (data outside the cap are also sensitive

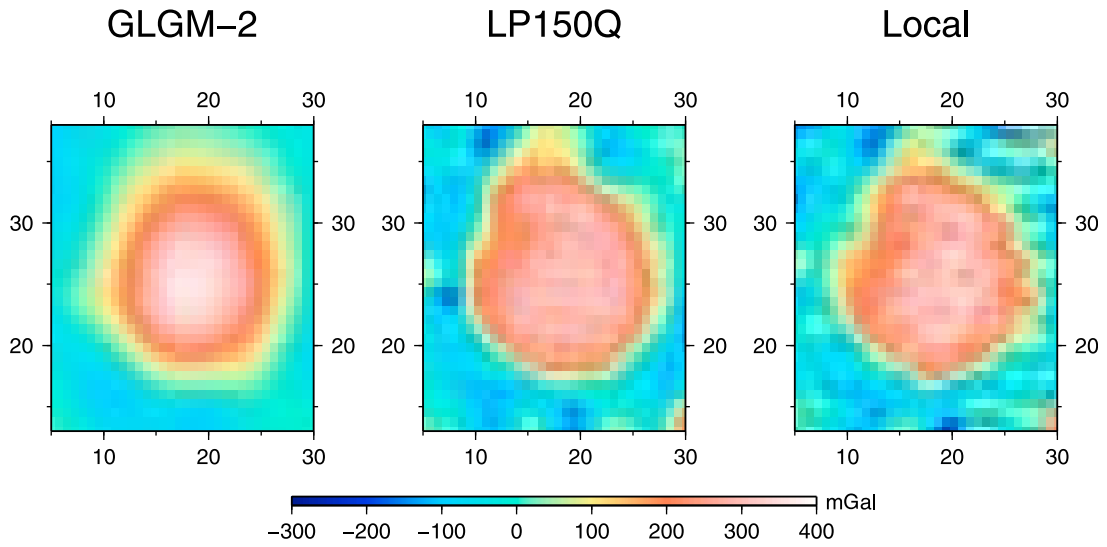

Figure 2. Free-air gravity anomalies over the Serenitatis area computed from GLGM-2, LP150Q, and the local solution. Each solution is expanded up to its maximum resolution in spherical harmonics, thus 70, 150, and 100, respectively.

to gravity features outside the area of interest that are not accounted for), but a comparison between the two solutions indicates where they are close to each other, and thus where boundary effects are smaller. The difference plot included in Figure 3 shows that in general the differences inside the 10° area are much smaller than the adjustments themselves, but they still show signal in what appears to be close to a zonal trend (positive and negative adjustments in the north-south direction). High-frequency differences with LP150Q can also be seen inside the mascon. These might stem from aliasing of higher degrees (note that the local solution presented here is up to degree and order 100 while the LP data have information at higher resolutions), but on the other hand, these were also somewhat visible in the results of *Goossens et al.* [2005b]. Finally, correlations between various solutions over the mascon area were also computed, and it was found that the local solution is closer to LP150Q's (the correlation between them is 94%) than GLGM-2's (a correlation with the local solution of 90%). The correlation between LP150Q and GLGM-2 is 89%.

4. Results for SPA Using SELENE Tracking Data

[23] The straightforward benchmark test served as a proof of concept, and it showed that the method as implemented, using Slepian functions, can indeed extract the extra information present in the tracking data. We now apply this same method to SELENE tracking data.

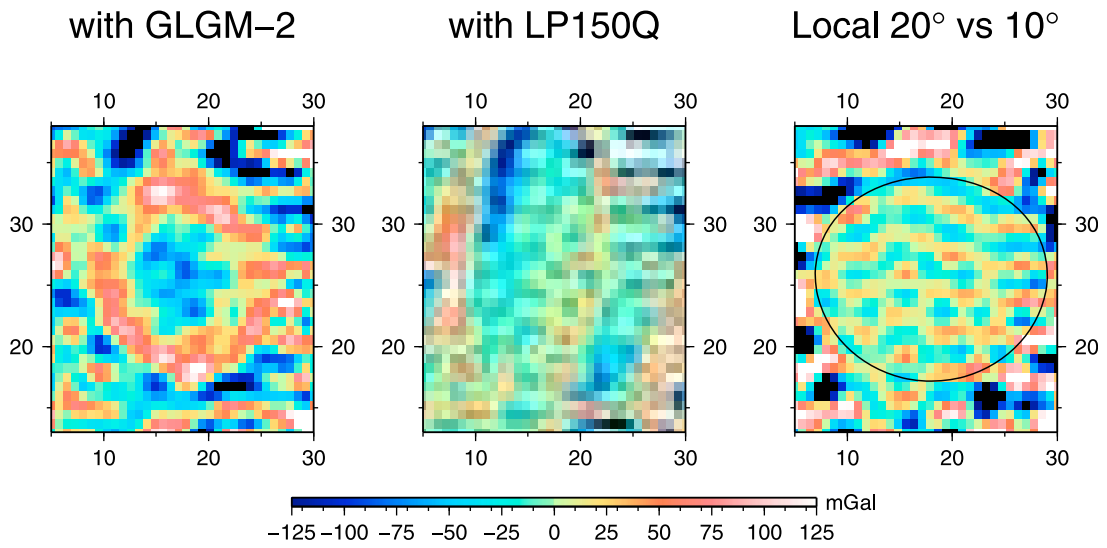

Figure 3. Differences in free-air gravity anomalies between the local solution and either GLGM-2 or LP150Q. To assess boundary effects, the difference between two local solutions with the functions concentrated in a spherical cap of either 20° or 10° are also plotted.

4.1. Processing of the SELENE Tracking Data

[24] We concentrate on the South Pole-Aitken (SPA) basin. As mentioned in section 2, we process the tracking data in the same way as was done for the SGM100h model [*Matsumoto et al.*, 2010], with the difference the a priori gravity field model that is being used (which was SGM100h itself in this analysis). Design matrices per arc are generated, including arc parameters such as initial state vector adjustments and measurement biases, and from them we select only data over the area of interest. All the parameters that are adjusted per arc are also included in the reduced design matrix. The arc lengths used varied per satellite [see also *Matsumoto et al.*, 2010]: for Rstar they were on average 2.6 days, while for the main satellite they were 12 hours (and 6 hours after a reaction wheel failure in July 2008). The orbits for Rstar and the main satellite were determined simultaneously. The arc parameters are eliminated by partitioning when the normal matrices are accumulated. The influence of these parameters is discussed further in section 5.1. We used the following data weights in our solution: 2 mm/s for main orbiter 2-way Doppler data, 1 mm/s for relay satellite Doppler data (due to different ground stations being used), and 1 mm/s for 4-way data.

[25] We adopt the coordinates of the center of the SPA basin as given by *Garrick-Bethell and Zuber* [2009], i.e., (191.1°E, 53.2°S). We include data in a spherical cap area with a radius of 45° around this center (this area is also indicated in Figure 1, which showed the SELENE 4-way residuals), and we also estimate the Slepian functions coefficients concentrated in this area, with a concentration factor of 10^{-8}, and an equivalent spherical harmonics resolution of 150 degrees and orders, which results in estimating 4,446 Slepian function coefficients (compared to 22,797 coefficients for a full spherical harmonics solution of the same resolution). This area is slightly larger than the SPA area itself, to account for boundary effects, which we discuss in section 4.3.

[26] Considering that the tracking data are obtained from SELENE's main orbiter in an orbit at 100 km above the lunar surface, this resolution is likely beyond the sensitivity of the data. We use this resolution because the use of Slepian functions allows us to estimate many fewer coefficients than when we would estimate an equivalent spherical harmonics model. Nevertheless, we found that we needed regularization for this data set to damp the amplitude in the estimated coefficients, despite the fact that local methods are often applied to circumvent the need for regularization. This need was to be expected however, mostly because of the main orbiter altitude at which the downward continuation of errors is substantial (as opposed to the LP extended mission results presented in the previous section, which were at a much lower altitude), but also from the amount of 4-way data available. For SELENE, 2-way data outnumbered 4-way data by a great amount [*Matsumoto et al.*, 2010]. The total number of data into our solution was 203,927 points, of which roughly 170,000 were 2-way data, and only 34,000 were 4-way data. The concentration factor (chosen to be 10^{-8} from an analysis of the representation error) affects the number of coefficients that will be estimated, but we found that changing this to 0.0001 (resulting in 3093 coefficients) did not take away the need to regularize the solution. Differences between solutions with these two concentration factors were small and located at the boundary.

[27] To regularize the inverse problem, we constrained each coefficient toward zero with an a priori uncertainty following Kaula's rule [*Kaula*, 1966], $\sigma_l = \beta/l^2$, with l the spherical harmonics degree, σ_l the uncertainty for the set of coefficients from the same degree, and β a constant. Since this is expressed in spherical harmonics, regularization was applied to the spherical harmonics normal matrix, after which the transformation following equation (5) was applied [see also *Han et al.*, 2009]. The constant we used was $3.6 \cdot 10^{-4}$, the same as was used for the SGM100h model [*Matsumoto et al.*, 2010]. We also tested other constants and a power law based on the gravity potential from uncompensated topography, as was also done by *Mazarico et al.* [2010], but we found that this did not influence the final results much, as the influence of the different regularization rules was confined to the higher degrees, where correlations with topography have dropped, see also results in section 4.3.

4.2. Local Gravity Results for SPA

[28] With the aforementioned processing, we obtained gravity adjustments over the SPA area as depicted in Figure 4 as free-air anomalies. The adjustments are in general small, between plus and minus 68 mGal, with an RMS of 17 mGal. Foremost, this indicates that the a priori model SGM100h already captures the information in the 4-way data well. The adjustments do show clear signals, with an outstanding circular anomaly signal which is located over the southern rim of the Apollo basin (location 36.1°S, 151.8°W, diameter 537 km). There is also a distinct north-south pattern visible in the adjustments. This trend follows the ground track of the satellites involved, which is also seen in other high resolution lunar gravity field models, especially over the farside when there are no direct tracking data available [e.g., *Konopliv et al.*, 2001]. In our case, we think this is mainly caused by the 2-way data. The line-of-sight geometry around the south pole is such that the 2-way data are likely to be less sensitive to radial gravity signals, since their line-of-sight is close to perpendicular to the radial direction there. For the 4-way data, the sensitivity depends on the exact geometry between the main orbiter and the relay satellite. The 4-way residuals are thought to describe mostly the remaining signal between these two, despite the data being integrated data over the various links. Because the relay satellite is in a higher orbit with the apolune over the lunar southern hemisphere, it should be less affected by gravity perturbations. This is also corroborated by small 2-way residuals for the relay satellite [see *Matsumoto et al.*, 2010]. In Figure 5 we plotted the angle between the radial direction, defined as the direction from the center of the Moon to the ground track point of the main orbiter in lunar-fixed coordinates, and the vector from the main satellite to the relay satellite. If this angle is small, the 4-way link between relay and main satellite is in line with the radial direction. Figure 5, however, shows that there are lots of tracks with a large angle, and they tend to correlate visually with the tracks in Figure 4. The histogram included in Figure 5 that shows the number of data points in angle bins of 5° also shows there are many data points with

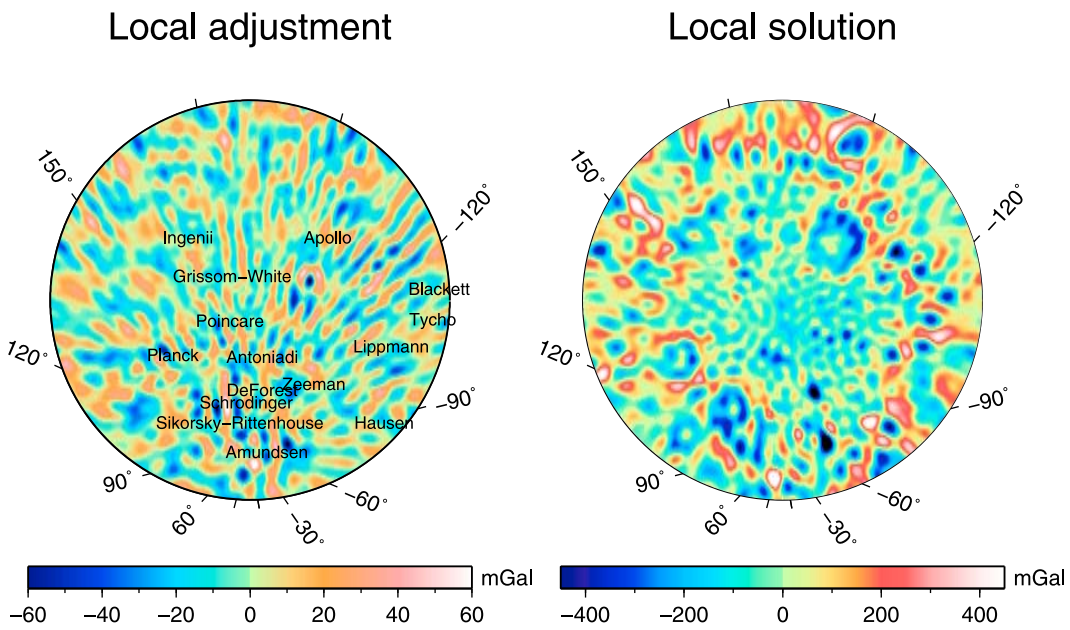

Figure 4. Adjustments in (free-air) gravity anomalies for the SPA region from the local method, together with the full solution (a priori SGM100h and local adjustment). The projection is gnomonic, centered around 191.1°E, 53.2°S. The names of several features on the lunar surface are also included in the adjustment plot, for reference. They are left-justified at the center of the feature, which means that the feature that is referred to is located at the start of its name.

large angles. This means that some of the tracks as seen in Figure 4 might also be due to 4-way geometry, although we emphasize that the 4-way data are not treated as line-of-sight data, but as the fully integrated data that they are. Nevertheless, with the 2-way data outnumbering the 4-way data by almost 5 to 1, there is a strong effect present on the solution, which we can not avoid with our current data set. It might be possible to mitigate this effect slightly by re-weighting the data, but we did not pursue this, since we wanted to weight the data as close as possible to the weights used for SGM100h. In our benchmark test in section 3 such an orbital track effect was not present, but this is likely because there

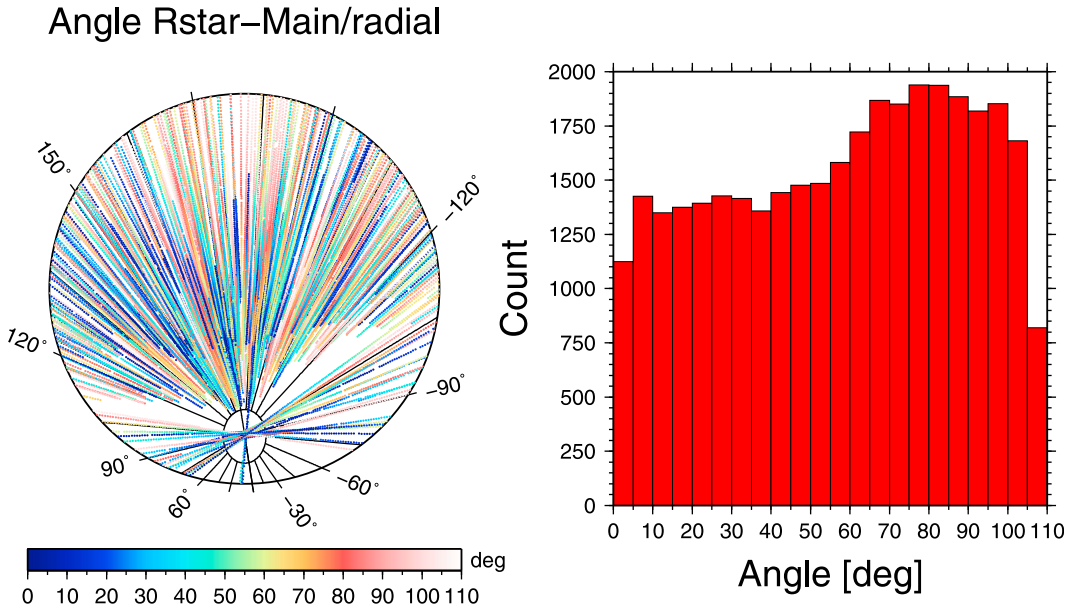

Figure 5. Geometry of the 4-way data over the SPA area. (left) The angle between the radial direction (taken as the ground track point of the main orbiter in lunar fixed coordinates) and the vector from the main satellite to the relay satellite are plotted, as well as (right) a histogram of counts of angles in 5° bins. Both plots show there is a substantial portion of the data with large angles, meaning less radial sensitivity.

the angle of line-of-sight with respect to the area of interest is different, and shorter arcs were used.

[29] Finally, there is also more variation in the free-air adjustments in the southern part of SPA. This is because there are more data available there, due to the inclusion of 2-way data around the south pole. These variations correlate with features such as Planck (57.9°S, 136.8°E, 314 km), Schrödinger (75°S, 132.4°E, 312 km) and Poincaré (56.7°S, 163.6°E, 319 km).

[30] When comparing the full solution (adjustment plus a priori field) to the a priori field only, the differences are more difficult to spot due to the different scales involved. When the two are displayed after each other in a loop (see auxiliary material), it becomes clear that the local adjustments modify the global a priori solution from SGM100h in such a way that several anomalies become less pronounced (e.g., the anomaly on the southern part of the ring around Apollo).[1] The modifications of the features mentioned in the previous paragraph can be seen as well. They are more clear when viewed in this way, since their full signal is visible, rather than the adjustments only. The interior area of SPA is also slightly modified.

[31] The adjustments themselves only show the differences with the a priori field, and obviously from those alone one can not tell whether there really is an improvement or not. We therefore evaluated the local solution by looking at the 4-way data fit. And in the next subsections, we evaluate the local solution in a geophysical sense by comparing gravity and topography.

[32] Data fit to the 4-way data for the new solution is difficult to evaluate, due to the local nature of the adjustments: the concentration of the Slepian functions means that they should be evaluated only within the area, whereas the arcs used in our dynamical approach cover the whole Moon. In order to have a direct comparison, instead of using the initial arcs used for the processing, we used the short-arc approach as applied in the benchmark test over Mare Serenitatis, in this case on a few selected tracks of 4-way data over the SPA area. We also included one pass of 4-way data obtained on January 30 of 2009, that filled in a remaining gap over the farside [*Matsumoto et al.*, 2010]. During this pass, the main orbiter flew at an average altitude of 60 km instead of 100 km. We found that in general the local solution results in a slightly better 4-way data fit than the a priori model. As can be expected from the adjustments, the improvements are small: from 0.2 mm/s to 0.17 mm/s, in an RMS sense. For the 4-way data taken on January 30, 2009, the improvement is from 0.24 mm/s to 0.18 mm/s. These values are smaller than the 4-way data fit values reported before by *Matsumoto et al.* [2010], because they are for short arcs. Overall, the local solutions thus improve the data fit, albeit only slightly. The data fit improvements however are thought to be indicative yet inconclusive, since the trackiness in the solution might be an artifact of remaining orbital signals, causing the fit to be better while inducing spurious signal into the gravity solution. Hence we look at different ways of validation.

[1]Auxiliary material data sets are available at ftp://ftp.agu.org/apend/je/2011je003831. Other auxiliary material files are in the HTML. doi:10.1029/2011JE003831.

4.3. Comparison With Lunar Topography

[33] For the lack of direct and independent measurements of gravity on the planets, which could be used for evaluation and calibration of the models, the correlation between gravity and topography is often used to evaluate a gravity field model, with the idea that especially at the higher degrees of the spectrum uncompensated topography contributes directly to the measured gravity field, and thus higher correlations indicate an improvement. Here, we use the methods of *Wieczorek and Simons* [2005] to compute correlations and admittance between gravity and topography over the SPA area, and we also look at spatial correlations between gravity adjustments and craters on the lunar surface.

[34] Figure 6 shows the correlation and admittance between various gravity models, and a topography model derived from SELENE LALT data [*Araki et al.*, 2009]. The results also include a gravity model named SGM150, which is a preliminary 150th degree and order spherical harmonics expansion of the lunar gravity field, based on the SELENE data that were used for SGM100h, and historical tracking data coming from Lunar Orbiters 1-3, the Apollo 15 and 16 sub-satellites (all satellites with non-polar inclinations), and all Lunar Prospector tracking data, including the extended mission data (which so far has not been included in the 100th degree and order SELENE models). LP extended mission data were processed in arc lengths of 2 days, using a data weight of 3 mm/s for Doppler data from January 1999 until May 1999, and a data weight of 6 mm/s for Doppler data from May 1999 until the end of the mission. This division was chosen following *Konopliv et al.* [2001], where different data weights were applied according to the location of the perilune of LP (over the nearside for the first half of the extended mission, and over the farside for the second half). SGM150 was furthermore estimated using a Kaula rule of $2.5 \cdot 10^{-4}/l^2$, slightly stricter than what we applied to our local solution, but the same as other global solutions of the same resolution [*Konopliv et al.*, 2001; *Mazarico et al.*, 2010].

[35] The results in Figure 6 show that the local solution has the highest correlations with topography. The differences are again not large, but they are pronounced for especially the degrees spanning $l = 60$–75. The trackiness in the adjustments (see Figure 4) does thus not affect the solution up to these degrees. After about degree 75, all solutions show a distinct drop in their correlation with topography, and this is likely because at this point the Kaula smoothing starts to become noticeable [*Matsumoto et al.*, 2010]. We used a spherical cap of 30° for the localization, in order to be safe from boundary effects in the local solution. While 30° seems conservative, the correlations are always better for the local solution for larger cap sizes, but the differences between the gravity solutions become less pronounced. This means that, as often in local inversions, one should be careful with the solution at the boundaries. We also discuss this further in this section, when correlating topography and adjustments spatially.

[36] At the higher end of the spectrum, beyond degree 90, SGM150 has better correlations than the local solution. This is probably due to the inclusion of the LP extended mission data into SGM150, showing that these data have an effect at the higher degrees (likely especially over the south pole,

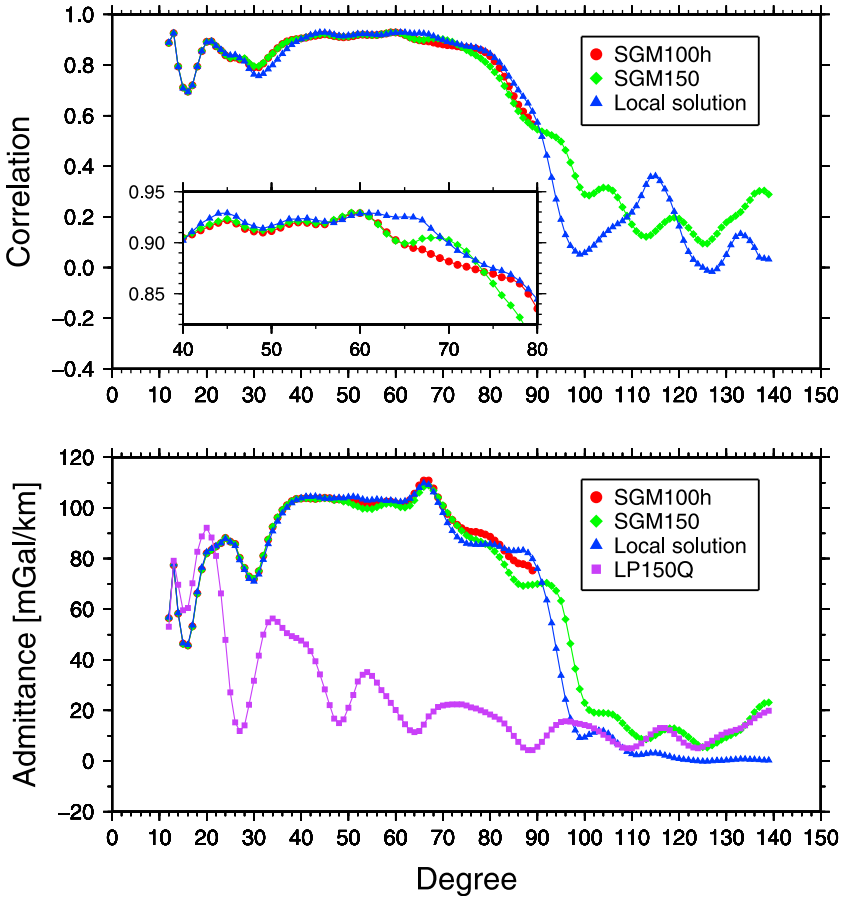

Figure 6. (top) Localized correlations and (bottom) admittance over the SPA area, for a spherical cap of 30°, for various gravity field models.

as the 2-way data accumulate there), although for both models, correlations are dropping for the higher degrees. We discuss the LP extended data further in section 5.

[37] The drop in correlations indicate that the solutions are losing their strength. The SELENE farside data assure that spherical harmonics models can be estimated up to degree and order 70 without the use of applying an a priori constraint [*Matsumoto et al.*, 2010]. It is also beyond this degree that the correlations with topography start to drop. This might lead one to wonder whether the data allow a 150th degree and order solution. However, a 100th degree and order local solution does not show the improved correlations as the 150th degree and order solution shown in Figure 6 does. This leads us to reason that even though the full resolution of 150 by 150 might not be exploited, increasing the resolution at least assures an internal distribution of the signal over the model coefficients such that overall the solution improves up to about degree 75. This was also corroborated by a 120 degree and order local solution that we tested, that showed the same correlations as the 150 degree and order local solution.

[38] The admittance values (the transfer function between gravity and topography) are also shown in Figure 6. They show slightly different values in the same range of degrees as the difference in correlations did. All models are quite steady and level off at a value slightly higher than 100 mGal/km. The local solution provides the most leveled and steady admittance value, at 104 mGal/km, whereas SGM100h reaches 102 mGal/km and SGM150 reaches 99 mGal/km. We also point out that Figure 6 shows a second plateau for the admittance values for the local solution, between degrees 70 and 90, with a value of 85 mGal/km, which is not as pronounced in the other solutions. For comparison, we also included the admittance between LP150Q and the LALT topography, indicating how admittance estimates have changed with the inclusion of SELENE farside data. Admittance values can be used to estimate the lithospheric thickness [e.g., *McKenzie and Nimmo*, 1997; *Crosby and McKenzie*, 2005].

[39] To assess the correlations with topography spatially, we investigated the correspondence between the local gravity adjustments and craters on the lunar surface. We did this by plotting the crater database of *Head et al.* [2010] (who produced a catalogue of impact craters ≥20 km in diameter on the lunar surface) on top of the adjustments evaluated between degrees l = 40–80, the result of which is shown in Figure 7. We chose this frequency band because between those degrees, the correlation with topography increased, as explained before. There is sometimes an offset between anomalies and craters, especially in the south-western part of the solution, which could be due to issues of data coverage or orbital errors, but for the larger part anomalies correlate

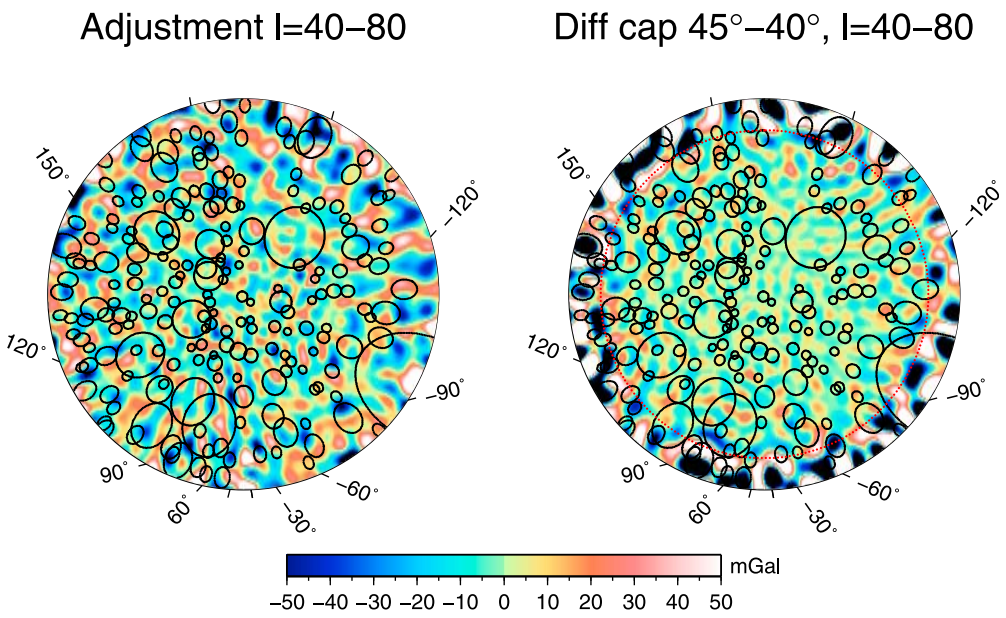

Figure 7. (left) Adjustments expressed as free-air gravity anomalies, in the frequency band that showed increased correlations with topography (l = 40–80), and (right) differences between two local solutions using either data in a cap of 45° or 40°, to assess boundary effects. The 40° boundary is indicated by the dotted red line. Craters with sizes ≥ 60 km, taken from *Head et al.* [2010], are indicated by black circles.

with craters. For example, the outstanding adjustment at the rim of Apollo follows a trail of small-scale craters rather well, and several smaller craters show negative adjustments. Figure 7 thus shows that the adjustments correspond to surface features, as was also inferred from increased correlations with topography.

[40] To assess the sensitivity of the adjustments with respect to the aforementioned boundary effects, we investigated the differences between two local solutions, based on localized functions in a cap of either 45° or 40° (and using data in those areas). These are also shown in Figure 7, again in the frequency band l = 40–80. As was the case with the results shown in section 3 when boundary effects were discussed, both solutions are affected by these effects. In addition, the difference plot in Figure 7 shows large differences outside the 40° area because the 40° solution is undefined there. Differences between the solutions are of a smaller amplitude than the adjustments themselves, but nevertheless the interior of the solution area is affected, with the biggest differences within several degrees of the 40° boundary. Some of the differences shown in Figure 7 correlate with small craters, although those are mostly on or outside of the 40° boundary. Overall however, the interior of the SPA area seems to be stable between both solutions, which makes us reasonably confident of the adjustments.

4.4. Bouguer Anomalies

[41] One of the advantages of the Slepian functions is their direct interchangeability with spherical harmonics, which means that it is relatively straightforward to derive properties other than free-air anomalies from the estimated coefficients. Using the local solution and LALT topography, we computed Bouguer anomalies for the SPA area, assuming a crustal density of 2800 kg/m^3 and leaving out corrections for mare basalt. Bouguer anomalies for the local solution and SGM100h are shown in Figure 8.

[42] The differences between the two solutions are more clear here than from the free-air anomalies, since the Bouguer anomalies have a wider range. Improvements in resolution for the local solution (while keeping in mind that the local solution is a larger expansion, in spherical harmonics) can be seen as certain features show more detail: for example, in the interior of SPA, around Apollo, Schrödinger, Planck, and in the vicinity of the Zeeman crater (75.2°S, 133.6°W, 190 km). Figure 9 shows the differences in Bouguer anomalies, with craters again plotted on top of the anomalies, and the aforementioned features are indicated as well. The differences are again most pronounced around the boundary areas, and while those are also influenced by boundary effects on the local solution, it should also be kept in mind that there is rougher topography at the edges of SPA (see Figure 1). Other differences correlate well with topographic surface features, as indicated by the agreement of anomaly differences with crater locations (although one should keep in mind that Bouguer anomalies were computed using topography data as input), especially in the southern part of SPA. This is possibly due to better data coverage there, despite trackiness induced by the 2-way data that has disappeared in the Bouguer adjustments.

[43] From Bouguer anomalies, the compensation state can be derived. As expected, our results here do not change the overall compensation state of SPA as found by previous analysis [e.g., *Zuber et al.*, 1994], since our adjustments are relatively small with respect to the overall signal. While the extremes in Bouguer anomalies in Figure 9 vary between ±200 mGal, the overall change is more modest, with an increase in the RMS of the Bouguer anomalies in the SPA area up to 289 mGal, from 283 mGal for SGM100h.

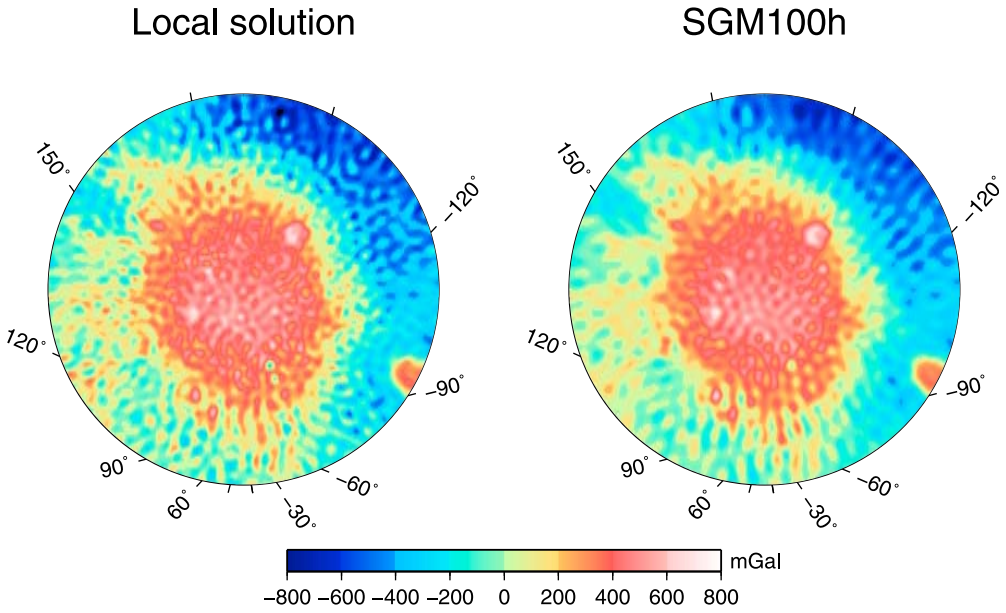

Figure 8. Bouguer anomalies over the SPA area from both the local solution and SGM100h.

Understanding SPA's compensation state may help in understanding how SPA contributed to the lunar orientation [*Garrick-Bethell and Zuber*, 2009], and local differences within SPA itself may point to modifications to the crustal structure that occurred after formation of SPA [e.g., *Neumann et al.*, 1996]. In that respect, it is interesting to note that from Figure 8 a modification in Bouguer anomalies corresponding to the Zeeman crater (indicated in Figure 9) stands out. Two small circular negative Bouguer anomalies close to the south pole can be seen clearly in the local solution, while they were less visible (and not negative) in the SGM100h solution. The lower of the two corresponds to the Zeeman crater, while the upper of the two is at least partly covered by it. We point out that Zeeman is one of the features where *Yamamoto et al.* [2010] found exposures of olivine, which could lead to a different Bouguer signal, and a signature in the Moho uplift (see below).

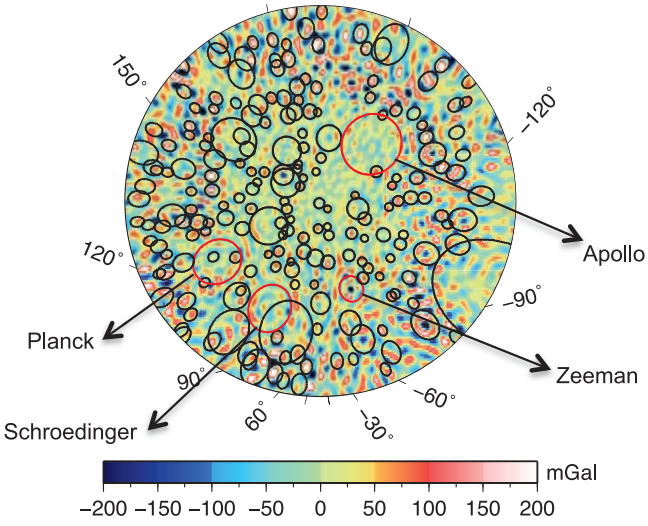

Figure 9. Difference in Bouguer anomalies over the SPA area between the local solution and SGM100h, with craters with sizes ≥ 60 km indicated.

[44] Finally, we tested how our new solution modifies the estimate of the Moho topography beneath the SPA basin. We compare our results with those presented by *Ishihara et al.* [2009] (which were based on a predecessor model of SGM100h, called SGM100g), and since those results were based on a global expansion of the gravity field, we transformed our local solution to an equivalent spherical harmonics expansion valid over the entire globe. We do this by simply generating free-air anomalies from the local solution within the SPA basin (in this case limited to a spherical cap of 32° radius to prevent boundary effects leaking into the solution), and from SGM100h outside the basin. We then estimate a global 100th degree and order model from these anomalies. This model has the same correlations with topography as the local model. There are some anomaly differences within the SPA basin when compared to the local solution, and this model does not take full advantage of the increased resolution of the local solution, but on the other hand, *Ishihara et al.* [2009] used SGM100g up to degree and order 70, and we also find that up to this degree our local solution has increased correlations with topography. In other words, the loss of resolution should have only a small effect. Local crustal thickness analysis might be applied in order to make more use of increased resolution.

[45] For determining the Moho topography, we expanded the models up to degree 80, using the same gravity inversion method as *Ishihara et al.* [2009]. Figure 10 shows the Moho topography for different gravity field models beneath SPA. Their differences are also included, and from these, the modification on the southern rim of the Apollo basin that was also found in the free-air anomalies clearly stands out. It should be noted however that the feature disappears in the local solution, making the Moho structure south of the rim of Apollo a little smoother. The modification in the Zeeman crater that was found in the Bouguer anomalies can also be

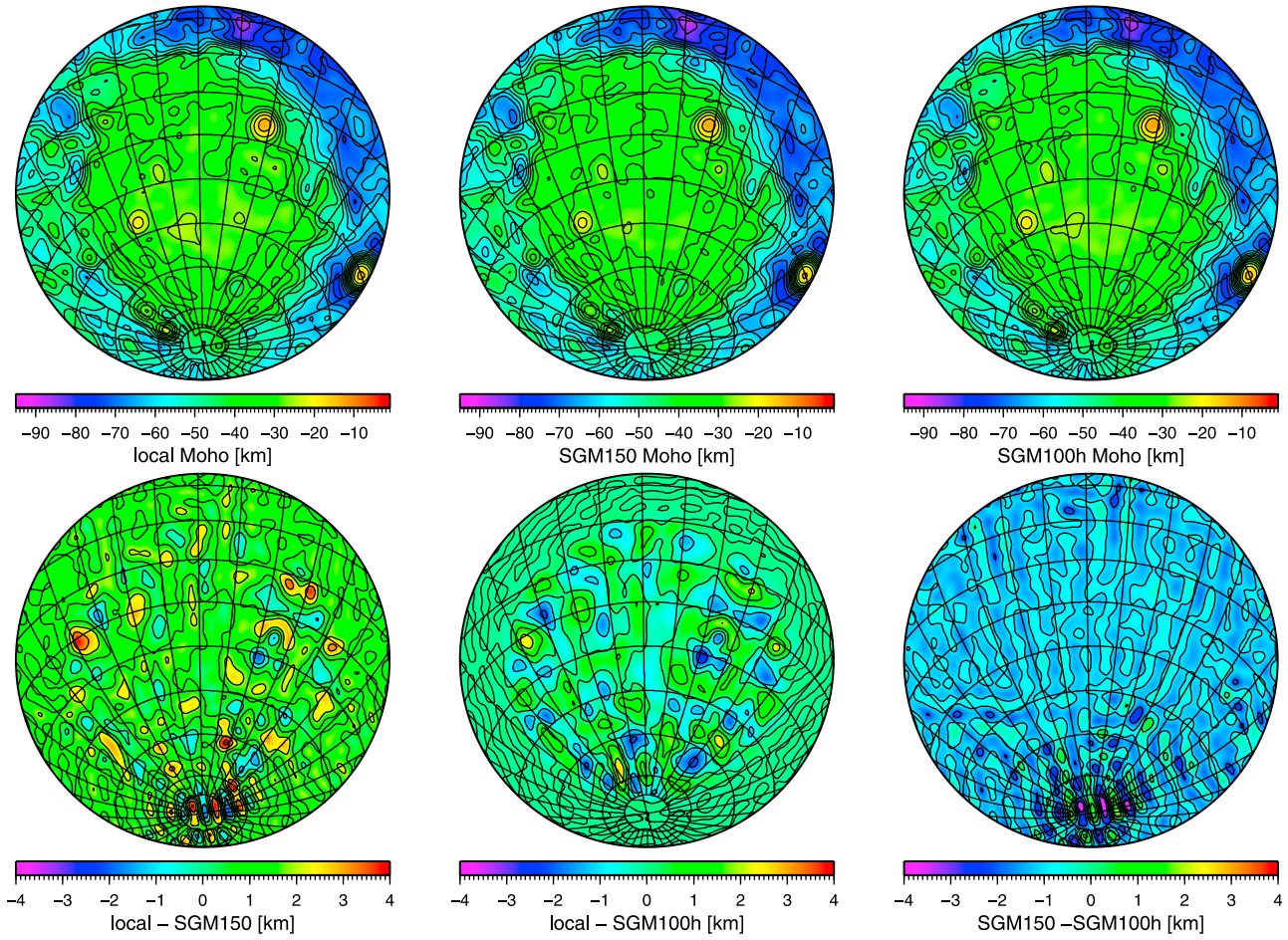

Figure 10. Moho topography beneath SPA using different gravity field models and their differences.

seen. From the differences only, it shows more uplift in the local model than it does for the global models, especially SGM150. However, our local solution does not seem to indicate a mantle plug associated with this area. Finally, the southern part of SPA is again affected most because there were more data there.

5. Discussion

[46] Here, we discuss the performance of the recovery method, with respect to specific choices we made, such as the choice of estimated parameters and the a priori model. We also briefly discuss the use of LP extended mission data.

5.1. State Vector Effects

[47] As mentioned in section 4.1, we formed the normal matrices per arc from the data over the SPA area, while including arc parameters (such as the adjustments to the initial states of the satellites involved, measurement biases and arc-dependent solar radiation pressure force model parameters). The integration of the orbit and computation of the measurements according the used models is then iterated, with the arc parameters adjusted per iteration (keeping the global parameters fixed) in order to fit to the tracking data, until convergence is reached. These arc parameters were then eliminated from the formed normal matrix by partitioning, during the aggregation of the separate normal matrices. We tested whether or not these parameters need to be included by also forming normal matrices using only the partial derivatives with respect to the gravity parameters. This is different from eliminating the arc parameters all together, since by choosing only the gravitational parameters, the correlations between arc and common parameters are not accounted for. We found however that the solutions using only the partials for the gravity coefficients did not show increased correlations with topography. Correlations in the range l = 60–75 dropped below those for SGM100h, and also those in the higher degrees (beyond 100) were negatively affected. Gravity anomaly differences between these two local solutions (with and without the arc parameters included) are mostly confined to the southern part of SPA. The solution using only the gravity partials also shows more trackiness in its free-air anomalies. This indicates that there are still state vector effects present that need to be accounted for in the solution. Again, this likely affects the 2-way Doppler data most, since these data have coverage limited to the southern part of SPA.

[48] During the partitioning step, the arc parameters are eliminated through back-substitution which involves the inverse of the sub-matrix containing the arc parameters [e.g., *Kaula*, 1966]. We use all the data in the two-day arcs to converge them, but using only the data over the area of interest to form the normal matrix might lead to numerical

instabilities in the inversion of especially the arc parameters part when the normal matrices are aggregated. This is done with the SOLVE software, which allows for a dynamical suppression in the Cholesky inversion of parameters that turn out to have poor observability (indicated by very small or even negative numbers on the diagonal). Inspection of the results has shown that this is sometimes the case, mostly for certain bias-parameters that were included, but occasionally also for state vector parameters. Since we wanted to include all available 4-way data, we did not exclude those normal matrices where this was the case from the solution.

5.2. Influence of the a Priori Gravity Field Model

[49] In order to test the sensitivity of the method with respect to the a priori model, we processed the same data using LP100K [*Konopliv and Yuan*, 1999] as the a priori gravity field model. In this case the a priori model is independent of the SELENE data, as LP100K is a 100th degree and order spherical harmonics model based on LP tracking data (and as such, a precursor to the LP165P and LP150Q models). This test is similar in extent to the benchmark test presented in section 3, in that we process the data with an independent model to test whether the information can be extracted from the data. For LP100K, the gravity field over the SPA region is much smoother than that described by SGM100h, and a basin such as Apollo is not circular in shape. Correlations with topography over the SPA area are also much lower than those for the SGM100h and SGM150 models, with a distinct low around degree 60 where the correlations are close to zero. The SELENE 4-way data show large residuals with respect to LP100K [*Namiki et al.*, 2009].

[50] We found that our local solution based on LP100K as a priori model resolves the structure within the SPA basin rather well. The Apollo, Planck and Ingenii features stand out much clearer in the local solution than they do in anomalies computed from LP100K. Yet there is also some orbital trackiness visible in the solution, and while correlations with topography improve drastically over those for LP100K, up to correlations of 0.89 for the range $l = 40$–70, they do not reach the levels as obtained by the global or local SELENE models, which is about 0.93 for the same range. This means that we can only adjust the a priori model to some extent, and that, unsurprisingly, we get the best solutions if we start with a model that already describes the data well. One should also keep in mind that the dynamical approach in processing the tracking data here assumes linearity, and that global spherical harmonics models are often determined from multiple iterations over the data. Due to the local nature of our representation of the gravity field, which should only be evaluated within the area of interest, we did not iterate our solutions, since that would require processing arcs which also cover the rest of the Moon, outside of SPA.

5.3. LP Extended Mission Data

[51] LP extended mission data are especially interesting for local nearside analysis, and they have been the focus of previous local and regional analyses. And since we have also included SELENE 2-way Doppler data beyond the south pole, LP extended mission data might be included as well. We processed the LP extended mission data in the same way as they were processed for the SGM150 model (see section 4.3). We again selected only data over the SPA area when adding them to our local solution. Since these data are not included in SGM100h, they showed large residuals, and this has a profound effect on the solution: it shows large unrealistic gravity anomaly fluctuations.

[52] When we compared various gravity models in terms of their correlations with topography (see section 4.3), we noted that the SGM150 model showed increased correlations at the higher degrees, likely coming from the influence of LP extended mission data. In order to bypass the large residuals in the LP extended mission data when we process them with SGM100h, we recomputed the local solution starting from SGM150 instead (which included the LP extended mission data), using both SELENE and LP extended mission data. The SELENE-only solution shows similar free-air anomalies and correlations as the local solution starting from SGM100h. When we include the LP extended mission data however, correlations with topography unfortunately drop again, and orbital trackiness starts to appear in the solutions. If we down-weight the LP extended mission data when combining the normal matrix with that of the SELENE data, the solution improves, but it does not lead to for example increased correlations when compared to the SELENE data-only solution. Sensitivity issues as discussed in section 4.2 might especially play an important role here, and thus the LP extended data were not included into our solutions.

6. Conclusions

[53] We have estimated adjustments to a global lunar gravity field model over a limited area, by representing the gravity field by means of localized basis functions. We applied Slepian basis functions, which are represented by linear combinations of standard spherical harmonics. This makes them relatively straightforward to use in combination with existing data processing strategies based on spherical harmonics. We process tracking data in the standard dynamical way, which means that we follow an integrated approach where the local adjustments are estimated from the tracking data residuals directly (as opposed to numerically differentiating the Doppler residuals to obtain accelerations). This is especially useful for tracking data that consist of the accumulated Doppler shift between different links, such as the SELENE 4-way data. We generate the design matrix (which describes the linearized relationship between the residuals and the estimated parameters) using only data over the area of interest. From these reduced design matrices we create normal matrices and aggregate them in the standard way. The normal matrix is then transformed from spherical harmonics into Slepian functions, and we only estimate those function coefficients with a concentration factor larger than a pre-set value, which means that only functions that have power in the area of interest are estimated. The estimation is done in a least-squares sense.

[54] A benchmark test for the gravity recovery method was conducted, using Lunar Prospector (LP) extended mission tracking data over the Mare Serenitatis area on the nearside of the Moon. The data were processed with a pre-LP lunar gravity field model (GLGM-2) that shows smoothed gravity anomalies over Serenitatis when compared with LP-based lunar gravity field models. The test showed that the method as implemented can extract the high

resolution information from the tracking data, as we found improved correlations with anomalies from a high resolution global lunar gravity field model using LP data.

[55] We then estimated adjustments to the 100th degree and order SGM100h model for the SPA area, using Slepian functions in a resolution equivalent to degree and order 150 in spherical harmonics over an area with a spherical cap of 45° radius, centered at (191.1°E, 53.2°S), resulting in the need to estimate 4,446 Slepian function coefficients (as opposed to the 22,797 needed for a full global spherical harmonics model). The use of a limited set of data (only those over the area of interest) also means that we can create our local solutions much faster than a global solution of equivalent resolution. We applied a Kaula rule of $3.6 \cdot 10^{-4}/l^2$ to this solution to prevent large fluctuations in gravity anomalies. We used SELENE tracking data, including 4-way data over the SPA area, and 2-way data slightly beyond the south pole of the Moon. Even though we estimate fewer coefficients, the resolution of the model and the satellite altitude of 100 km are such that smoothing is required. An investigation into the effects of choosing data only over the area of interest showed that the solutions are generally affected up to a few degrees into the area of interest.

[56] The adjustments are small in general, between plus and minus 68 mGal with an RMS of 17 mGal. Foremost, this indicates that the a priori model SGM100h captures the information in the 4-way data well. Our new local solution shows increased correlations with high-resolution lunar topography, and admittance values that are slightly different and more leveled when compared to those from global models using the same SELENE data. Free-air anomaly adjustments, evaluated in the frequency band l = 40–80 (where the increase in correlations with topography was concentrated) correlate with craters on the lunar surface. Since our local solution is easily transformed into spherical harmonics, we also computed Bouguer anomalies. The local solution shows an increased resolution inside the SPA area, and differences with Bouguer anomalies from the global models correlate well with topographic surface features. The overall compensation state of SPA as found by previous analysis is not changed by our results, since we mostly adjust the global lunar gravity field models at their short-wavelength components. The Moho structure beneath the SPA basin is slightly modified by our solution, most notably at the southern rim of the Apollo basin, where a previously outstanding feature now appears smooth. We also found modifications in Moho structure and Bouguer anomalies for the area corresponding to the Zeeman crater (where olivine exposures were found).

[57] We demonstrated that the method can complement global solutions by refining them over areas where data are more dense. This might be especially of interest for future planetary missions such as GRAIL [*Zuber et al.*, 2008], where the lunar gravity field will be mapped from low-low satellite tracking data. While it is outside of the scope of this work to do a full analysis, such a data type is highly sensitive to local gravity field variations, and thus suitable for a local method such as presented here.

[58] The local solution over the SPA area that we presented here is made publicly available as a set of normalized spherical harmonics coefficients through the RISE Data Archive Web site, which can be found at http://www.miz.nao.ac.jp/rise-pub/en.

[59] **Acknowledgments.** We thank the Planetary Geodynamics Laboratory of NASA/GSFC for providing the GEODYN II/SOLVE software, and we are especially grateful to David Rowlands and Frank Lemoine for discussions concerning the software. We thank Mark Wieczorek for comments on the manuscript, particularly those concerning the localization procedures. The localization transformations applied in this work make extensive use of his SHTOOLS library, which is freely available from "http://www.ipgp.fr/∼wieczor/SHTOOLS/SHTOOLS.html". We also acknowledge support from Noriyuki Namiki (PERC, Chiba Institute of Technology, Japan) and Takahiro Iwata (ISAS/JAXA, Japan). Two anonymous reviewers are thanked for their comments which helped improve this manuscript. All figures were generated with the free Generic Mapping Tools (GMT) software [*Wessel and Smith*, 1991]. This work was supported by Grant-in-Aid for Scientific Research (to S.S.) (grant 20244073) from the Japan Society for the Promotion of Science.

References

Anderson, J. D., G. Schubert, R. A. Jacobson, E. L. Lau, W. B. Moore, and J. L. Palguta (2004), Discovery of mass anomalies on Ganymede, *Science*, *305*, 989–991.

Araki, H., et al. (2009), Lunar global shape and polar topography derived from Kaguya-LALT laser altimetry, *Science*, *323*, 897–900, doi:10.1126/science.1164146.

Barriot, J. P., and G. Balmino (1992), Estimation of local planetary gravity fields using line of sight gravity data and an integral operator, *Icarus*, *99*(1), 202–224.

Binder, A. B. (1998), Lunar Prospector: Overview, *Science*, *281*, 1475–1476.

Crosby, A., and D. McKenzie (2005), Measurements of the elastic thickness under ancient lunar terrain, *Icarus*, *173*, 100–107, doi:10.1016/j.icarus.2004.07.017.

Garrick-Bethell, I., and M. T. Zuber (2009), Elliptical structure of the lunar South Pole-Aitken basin, *Icarus*, *204*, 399–408, doi:10.1016/j.icarus.2009.05.032.

Goossens, S., P. N. A. M. Visser, and B. A. C. Ambrosius (2005a), A method to determine regional lunar gravity fields from earth-based satellite tracking data, *Planet. Space Sci.*, *53*, 1331–1340.

Goossens, S., P. N. A. M. Visser, K. Heki, and B. A. C. Ambrosius (2005b), Local gravity from Lunar Prospector tracking data: Results for Mare Serenitatis, *Earth Planets Space*, *57*(11), 1127–1132.

Grünbaum, F. A., L. Longhi, and M. Perlstadt (1982), Differential operators commuting with finite convolution integral operators: some non-Abelian examples, *SIAM J. Appl. Math.*, *42*(5), 941–955.

Han, S.-C. (2008), Improved regional gravity fields on the Moon from Lunar Prospector tracking data by means of localized spherical harmonic functions, *J. Geophys. Res.*, *113*, E11012, doi:10.1029/2008JE003166.

Han, S.-C., E. Mazarico, and F. G. Lemoine (2009), Improved nearside gravity field of the Moon by localizing the power law constraint, *Geophys. Res. Lett.*, *36*, L11203, doi:10.1029/2009GL038556.

Han, S.-C., E. Mazarico, D. D. Rowlands, F. G. Lemoine, and S. Goossens (2011), New analysis of Lunar Prospector radio tracking data brings the nearside gravity field of the Moon with an unprecedented resolution, *Icarus*, *215*, 455–459, doi:10.1016/j.icarus.2011.07.020.

Head, J. W., III, C. I. Fasset, S. J. Kadish, D. E. Smith, M. T. Zuber, G. A. Neumann, and E. Mazarico (2010), Global distribution of large lunar craters: implications for resurfacing and impactor populations, *Science*, *329*, 1504–1507, doi:10.1126/science.1195050.

Ishihara, Y., S. Goossens, K. Matsumoto, H. Noda, H. Araki, N. Namiki, H. Hanada, T. Iwata, S. Tazawa, and S. Sasaki (2009), Crustal thickness of the Moon: Implications for farside basin structures, *Geophys. Res. Lett.*, *36*, L19202, doi:10.1029/2009GL039708.

Kato, M., S. Sasaki, Y. Takizawa, and the Kaguya project team (2010), The kaguya mission overview, *Space Sci. Rev.*, *154*, 3–19, doi:10.1007/s11214-010-9678-3.

Kaula, W. M. (1966), *Theory of Satellite Geodesy: Applications of Satellites to Geodesy*, Blaisdell Publ., Waltham, Mass.

Konopliv, A. S., and D. N. Yuan (1999), Lunar Prospector 100th degree gravity model development, *Lunar Planet. Sci. Conf.*, *XXX*, Abstract 1067.

Konopliv, A. S., S. W. Asmar, E. Carranza, W. L. Sjogren, and D. N. Yuan (2001), Recent gravity models as a result of the Lunar Prospector mission, *Icarus*, *150*, 1–18.

Lemoine, F. G. R., D. E. Smith, M. T. Zuber, G. A. Neumann, and D. D. Rowlands (1997), A 70th degree lunar gravity model (GLGM-2) from Clementine and other tracking data, *J. Geophys. Res.*, *102*, 16,339–16,359.

Matsumoto, K., et al. (2010), An improved lunar gravity field model from SELENE and historical tracking data: revealing the farside gravity features, *J. Geophys. Res.*, *115*, E06007, doi:10.1029/2009JE003499.

Mazarico, E., F. G. Lemoine, S.-C. Han, and D. E. Smith (2010), GLGM-3, a degree 150 lunar gravity model from the historical tracking data of NASA Moon orbiters, *J. Geophys. Res.*, *115*, E05001, doi:10.1029/2009JE003472.

McKenzie, D., and F. Nimmo (1997), Elastic thickness estimates for Venus from line of sight accelerations, *Icarus*, *130*, 198–216.

Menke, W. (1989), *Geophysical Data Analysis: Discrete Inverse Theory*, *Int. Geophys. Ser.*, vol. 45, Academic, San Diego, Calif.

Muller, P. M., and W. L. Sjogren (1968), Mascons: Lunar mass concentrations, *Science*, *161*, 680–684.

Namiki, N., et al. (1999), Selenodetic experiments of SELENE: Relay subsatellite, differential VLBI and laser altimeter, *Adv. Space Res.*, *23*(11), 1817–1820.

Namiki, N., et al. (2009), Farside gravity field of the Moon from four-way Doppler measurements of SELENE (Kaguya), *Science*, *323*, 900–905, doi:10.1126/science.1168029.

Neumann, G. A., M. T. Zuber, D. E. Smith, and F. G. Lemoine (1996), The lunar crust: Global structure and signature of major basins, *J. Geophys. Res.*, *101*, 16,841–16,863.

Palguta, J., J. D. Anderson, G. Schubert, and W. B. Moore (2006), Mass anomalies on Ganymede, *Icarus*, *180*(2), 428–441, doi:10.1016/j.icarus.2005.08.020.

Pavlis, D. E., S. Poulose, and J. J. McCarthy (2006), GEODYN II system description, vol. 1-5, contractor report, SGT Inc., Greenbelt, Md.

Rowlands, D. D., S. B. Luthcke, J. J. McCarthy, S. M. Klosko, D. S. Chinn, F. G. Lemoine, J.-P. Boy, and T. J. Sabaka (2010), Global mass flux solutions from GRACE: A comparison of parameter estimation strategies - Mass concentrations versus Stokes coefficients, *J. Geophys. Res.*, *115*, B01403, doi:10.1029/2009JB006546.

Simons, F. J., and F. A. Dahlen (2006), Spherical slepian functions and the polar gap in geodesy, *Geophys. J. Int.*, *166*(3), 1039–1061, doi:10.1111/j.1365-246X.2006.03065.x.

Simons, F. J., F. A. Dahlen, and M. A. Wieczorek (2006), Spatiospectral localization on a sphere, *SIAM Rev.*, *48*(3), 504–536, doi:10.1137/S0036144504445765.

Sugano, T., and K. Heki (2004a), High resolution gravity anomaly map from the Lunar Prospector line-of-sight acceleration data, *Earth Planets Space*, *56*, 81–86.

Sugano, T., and K. Heki (2004b), Isostasy of the Moon from high-resolution gravity and topography data: Implication for its thermal history, *Geophys. Res. Lett.*, *31*, L24703, doi:10.1029/2004GL022059.

Ullman, R. (2002), SOLVE program, user's guide, Raytheon STX, Greenbelt, Md.

Wessel, P., and W. H. F. Smith (1991), Free software helps map and display data, *EOS Trans. AGU*, *72*, 441.

Wieczorek, M. A., and F. J. Simons (2005), Localized spectral analysis on the sphere, *Geophys. J. Int.*, *162*, 655–675, doi:10.1111/j.1365-246X.2005.02687.x.

Yamamoto, S., et al. (2010), Possible mantle origin of olivine around lunar impact basins detected by SELENE, *Nat. Geosci.*, *3*, 533-536, doi:10.1038/ngeo897.

Zuber, M. T., D. E. Smith, F. G. Lemoine, and G. A. Neumann (1994), The shape and internal structure of the Moon from the Clementine mission, *Science*, *266*, 1839–1843.

Zuber, M. T., D. E. Smith, L. Alkalai, D. H. Lehman, M. M. Watkins, and the GRAIL Team (2008), Outstanding questions on the internal structure and thermal evolution of the Moon and future prospects from the GRAIL mission, *Lunar Planet. Sci.*, *XXXIX*, Abstract 1074.

S. Goossens, CRESST/Planetary Geodynamics Laboratory, NASA Goddard Space Flight Center, 8800 Greenbelt Rd., Greenbelt, MD 20771, USA. (sander.j.goossens@nasa.gov)

Y. Ishihara, K. Matsumoto, and S. Sasaki, RISE Project, National Astronomical Observatory of Japan, 2-12 Hoshigaoka, Mizusawa, Oshu, Iwate 023-0861, Japan. (ishihara@miz.nao.ac.jp; matumoto@miz.nao.ac.jp; sho@miz.nao.ac.jp)